10-7-2014

Numerical Simulation of the Long-Range Propagation of Gravity Wave Packets at High Latitudes

C. J. Heale
Embry-Riddle Aeronautical University, HEALEC@erau.edu

J. B. Snively
Embry-Riddle Aeronautical University, snivelyj@erau.edu

M. P. Hickey
Embry-Riddle Aeronautical University, hicke0b5@erau.edu

AGU PUBLICATIONS

JGR

Journal of Geophysical Research: Atmospheres

RESEARCH ARTICLE

10.1002/2014JD022099

Key Points:
- Long-range propagation is favorable for waves trapped in the stratosphere
- Waves in the mesosphere may be a result of leakage from stratospheric duct
- Short-period waves are more likely to undergo sustained horizontal propagation

Correspondence to:
C. J. Heale,
healec@my.erau.edu

Citation:
Heale, C. J., J. B. Snively, and M. P. Hickey (2014), Numerical simulation of the long-range propagation of gravity wave packets at high latitudes, *J. Geophys. Res. Atmos.*, *119*, doi:10.1002/2014JD022099.

Received 29 MAY 2014
Accepted 29 AUG 2014
Accepted article online 2 SEP 2014

Numerical simulation of the long-range propagation of gravity wave packets at high latitudes

C. J. Heale[1], J. B. Snively[1], and M. P. Hickey[1]

[1]Department of Physical Sciences, Embry-Riddle Aeronautical University, Daytona Beach, Florida, USA

Abstract We use a 2-D, nonlinear, time-dependent numerical model to simulate the propagation of wave packets under average high latitude, winter conditions. We investigate the ability of waves to propagate large horizontal distances, depending on their direction of propagation relative to the average modeled ambient winds. Wave sources were specified to represent the following: (1) the most common wave parameters inferred from observations of Nielsen et al. (2009) (18 km λ_x, 7.5 min period), (2) waves consistent with the average phase speed observed (40 m/s) but outlying horizontal wavelength and period values (40 km λ_x, 17 min period), and (3) waves which would be subject to strong ducting as suggested by Snively et al. (2013) (25 km λ_x, 6.7 min period). We find that wave energy density was sustained over large horizontal distances for waves ducted in the stratosphere. Waves traveling against winds in the upper stratosphere/lower mesosphere are more likely to be effectively ducted in the stratosphere and travel large horizontal distances, while waves which escape in the form of leakage are more likely to be freely propagating above 80 km altitude. Waves propagating principally in the direction of the stratopause winds are subject to weaker stratospheric ducting and thus increased leakage of wave energy density from the stratosphere. However, these waves are more likely to be subject to reflection and ducting at altitudes above 80 km based upon the average winds chosen. The wave periods that persist at late times in both the stratosphere and the mesosphere and lower thermosphere (MLT) range from 6.8 to 8 min for cases (1) and (3). Shorter-period waves tend to become trapped in the stratosphere, while longer-period waves can dissipate in the thermosphere with little reflection or trapping. It is suggested that the most common scenario is of partial ducting, where waves are observed in the airglow after they leak out of the stratosphere, especially at large horizontal distances from the source. Stratospheric ducting and associated leakage can contribute to a periodic and horizontally distributed forcing of the MLT.

1. Introduction

Gravity waves have a significant effect on the mesosphere and lower thermosphere (MLT) region, accounting for up to 70% of the momentum budget [*Fritts and Vincent*, 1987]. Waves can deposit their momentum and energy in this region through viscous dissipation and wave breaking [*Pitteway and Hines*, 1963; *Fritts et al.*, 2006; *Yigit et al.*, 2008; *Fritts and Lund*, 2011; *Waterscheid and Hickey*, 2011]. Dissipation effects below 100 km, due to kinematic viscosity and thermal conduction, are not significant, and gravity waves can propagate with very little attenuation [*Pitteway and Hines*, 1963]. However, above this altitude, gravity waves which are not subject to breaking will dissipate at differing rates and altitudes depending upon their phase speeds [e.g., *Vadas*, 2007, and references cited within].

Observational and numerical studies show that waves can become trapped in ducts formed by the thermal structure of the atmosphere as well as winds [e.g., *Taylor et al.*, 1997; *Walterscheid et al.*, 1999; *Hickey*, 2001; *Walterscheid et al.*, 2001; *Hecht et al.*, 2001; *Snively and Pasko*, 2003; *Suzuki et al.*, 2004; *Snively and Pasko*, 2008; *Walterscheid and Hickey*, 2009]. Since a duct acts like a waveguide, trapping waves between two altitudes, ducted waves can travel over large horizontal distances without experiencing significant dissipation [e.g., *Stobie et al.*, 1983; *Walterscheid et al.*, 2001, and references cited within]. By this mechanism, gravity waves have been observed to travel and span distances up to 1800 km in airglow imagers [*Suzuki et al.*, 2013]. It has been suggested that waves observed in imager data could have originated from sources thousands of kilometers away [*Pautet et al.*, 2005]. However, it is not known how far a gravity wave can propagate horizontally before being dissipated, especially when considering the effects of changing winds and atmospheric background conditions.

Studies such as *Isler et al.* [1997] have noted the ubiquitous nature of gravity waves in airglow measurements at mesospheric heights. They suggest that the percentage of ducted waves, which have the ability to travel large distances, can be as high as ~75% at midlatitudes. The fraction of ducted waves depends strongly on the site where the measurements are taken. *Nielsen et al.* [2012] found that a much smaller fraction of ~18% was ducted or evanescent at high latitudes and note that the higher percentage of freely propagating waves (~82% in 2000) are more likely to reach thermospheric heights and dissipate and thus form an important source of energy transfer to the MLT. This is suggested as a result of the weaker winds and tides at high latitudes [e.g., *Hibbins et al.*, 2006]. Despite differences reported in direction of propagation and the fraction of ducted waves, studies tend to find very similar wave parameters. Horizontal wavelengths typically range between 20 and 50 km, with periods ranging from 5 to 15 min [*Nielsen et al.*, 2009].

Simulations have shown successful far-field thermal ducting of gravity waves generated by linear tropospheric forcing [e.g., *Walterscheid et al.*, 2001] and nonlinear breaking of tropospheric generated waves [*Snively and Pasko*, 2003]. In addition, *Yu and Hickey* [2007b] investigated the energy flux over time of ducted waves, finding that waves observed in the mesosphere may be observable at even greater distances in the stratosphere. *Yu and Hickey* [2007a] also noted a periodic forcing of the MLT as a result of duct leakage. *Snively et al.* [2013] used a 1-D full wave model to study the phase speed and period parameter space over Halley, using the same ambient atmosphere parameters that are used in the present study. They found that although waves may be freely propagating in the mesosphere, there could be occurrences of ducting or reflection at other altitudes that may contribute to long-range wave propagation.

Strong ducting relies on approximate integer numbers of half wavelengths fitting within the vertical scale of the duct, such that the energy flux approaches zero at the boundaries and standing waves form [*Walterscheid et al.*, 2001]. In reality, ducts will leak energy [*Hickey*, 2001] and the amplitudes of the waves inside the duct will decay over time. Any wave energy leaking from the duct may be dissipated higher in the atmosphere; if the depth of the evanescent (where the vertical wave number, $m^2 < 0$) region outside of the duct is small compared to the scale of wave decay, the wave can tunnel out of the duct and continue to propagate vertically [*Nappo*, 2002; *Sutherland and Yewchuk*, 2004; *Simkhada et al.*, 2009].

In addition to thermal ducting, winds can Doppler shift the intrinsic frequency ($\Omega = \omega - kU$, where ω is the ground relative frequency, k is the horizontal wave number, and U is the background horizontal wind) of a wave to the local buoyancy frequency, causing the wave to become evanescent and reflect. Via this mechanism, certain wind profiles can create evanescent regions at two different altitudes, with a region of propagation in between them leading to Doppler ducts [*Chimonas and Hines*, 1986; *Isler et al.*, 1997]. The shift in the intrinsic frequency of the wave is dependent upon the propagation direction. If the wind is in the direction of wave propagation, then the intrinsic frequency shifts to a lower value, whereas if the wind is in the opposite direction, then the intrinsic frequency shifts to a higher value [*Nappo*, 2002]. Therefore, the direction of wave propagation relative to the wind can affect its ability to travel large horizontal distances, leading to anisotropies in observed wave directionality [*Hecht et al.*, 2001; *Walterscheid et al.*, 2001].

While waves can be trapped in narrow ducting regions, they can also experience a "deep" ducting caused by partial wave reflection in the thermosphere [*Tuan and Tadic*, 1982]. In this case a wave can simply bounce between the reflection level and the ground, while losing amplitude over time as part of the wave is transmitted into, and thus dissipated, within the thermosphere [*Chimonas and Hines*, 1986; *Wang and Tuan*, 1988]. This process appears likely to play a role at high latitudes [*Snively et al.*, 2013].

In this paper, we aim to investigate the nature of long-range gravity wave propagation under average background atmospheric thermal and meridional wind conditions at high latitudes by using the three case studies described in section 2. We use both periodic and horizontally extended domains to analyze the effectiveness of ducting and reflection, energy distributions over time, and momentum flux distributions under averaged background temperature and wind structures. We also assess the effect of wind direction relative to wave propagation direction.

The paper is organized as follows: section 2 presents an outline of the model, ambient atmosphere, and wave parameters used in the simulation. It also includes theoretical background and a description of the simulation space and forcing conditions. Section 3 presents results of the periodic domain runs and Fourier analysis of frequencies present with altitude. Section 4 presents the results of the horizontally extended

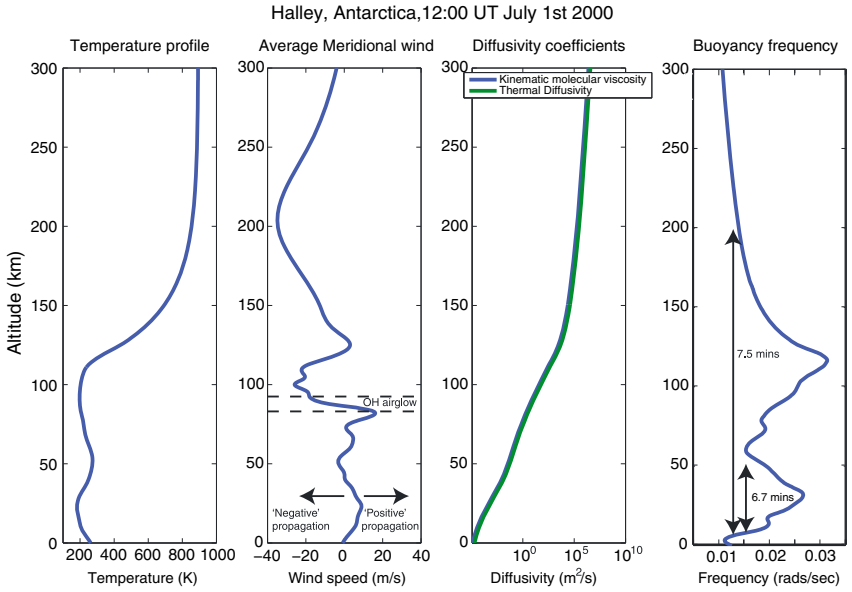

Figure 1. Temperature, average meridional wind, viscous profiles, and buoyancy frequency for 1 July 2000 over Halley, Antarctica.

simulations for each of the three source configurations as well as corresponding kinetic energy density plots. Section 5 investigates the momentum flux and body forcing distributions and time dependence. Finally, sections 6 and 7 will summarize our results, discussion, and conclusions.

2. Numerical Model and Theory

2.1. Governing Equations and Ambient Atmosphere

The 2-D numerical model utilizes a modified set of the Clawpack libraries [*Clawpack Development Team*, 2014], in the form described by *Snively and Pasko* [2008]. The equations solved are the nonlinear, fully compressible, Euler equations with the inclusion of two separately solved equations describing the effects of molecular viscosity and thermal conductivity with a Prandtl number of 0.7. For full details see *Heale et al.* [2014].

We investigate the propagation of gravity waves with characteristics reported by *Nielsen et al.* [2009] under averaged background atmospheric conditions over Halley, Antarctica (latitude: 76°S, longitude: 27°W). As *Nielsen et al.* [2009] reported predominantly southward propagating waves (particularly in July), we consider only meridional wave propagation and meridional background winds. Our atmospheric profile (shown in Figure 1) is specified using NRLMSISE-00 [*Picone et al.*, 2002] for 1 July 2000 at 12:00 U.T. The background winds are specified by a diurnal average (based on 1 h intervals) for the same day using HWM07 [*Drob et al.*, 2008]. Solar conditions are taken to be typical, with $A_p = 4$ and $F_{10.7} = F_{10.7A} = 150$. These parameters coincide with those of *Snively et al.* [2013]. Simulations were performed for waves propagating in both directions relative to the wind and are referred to as "negative" propagation (specified with $-k$) and "positive" propagation (specified with $+k$) directions. While it is conceivable that these may correspond to southward ($-k$) and northward (k) propagation respectively, the winds change noticeably over the course of a day, and thus, we cannot draw any conclusions about actual wave direction constraints for any instant of time based on our averaged winds. Instead, we seek to understand the wind conditions that may be favorable for long-range propagation and the associated wave parameters.

2.2. Wave Parameters and Case Studies

We simulate three case studies: (1) waves with parameters similar to the average wave parameters observed in *Nielsen et al.* [2009] (horizontal wavelength $\lambda_x = 18$ km, observed period $\tau = 7.5$ min, and $c_p = 40$ m/s). (2) Waves with the average observed phase speed, but with periods and wavelengths which are toward the tail of the distribution ($\lambda_x = 40$ km, $\tau = 17$ min, and c_p ~40 m/s). (3) Waves that are predicted to be favored for long-range propagation ($\lambda_x = 25$ km and $\tau = 6.7$ min) [*Snively et al.*, 2013].

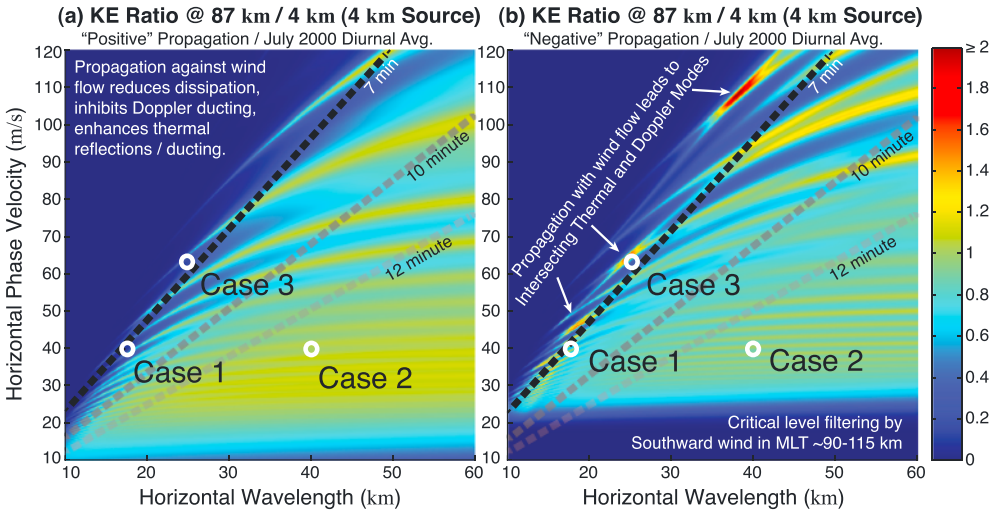

Figure 2. Kinetic energy ratio as a function of the phase speed-horizontal wavelength parameter space on 1 July 2000 over Halley, Antarctica.

Parameters for the cases chosen are illustrated in Figure 2, which is derived from the figures presented by *Snively et al.* [2013]. Figure 2 shows the kinetic energy ratio at 87 km altitude relative to 4 km altitude averaged over ±4 km, as a function of the phase speed-horizontal wavelength parameters space. The background atmosphere and winds are identical to those used by *Snively et al.* [2013], and the results are produced using high-resolution runs from a 1-D steady state full wave model [*Walterscheid and Hickey*, 2009]. The ratio of kinetic energy, as defined above, gives an indication of the enhancement or dissipation of a given wave in the airglow region relative to the source. Ratios greater than one suggest the accumulation of wave energy, which is most likely due to trapping or ducting of the wave, in the mesosphere, while values less than one suggest dissipation of the wave (or lack of accumulation). The cases chosen are indicated by circles on the plots, with case (3) chosen because it falls in a region of the parameter space where the kinetic energy ratio is large (~2), suggesting that ducting conditions are especially favorable.

2.3. Numerical Domain and Wave Forcing

The periodic boundary simulations force the horizontal extent of the domain to be the size of exactly one horizontal wavelength. The domain is set to be λ_x km × 300 km with a 0.5 km resolution in x and z. Frames are output every 60 s with a typical total simulation time of 300 min. The bottom boundary is set to be closed (reflecting), the sides are periodic, and the top is open (allows waves to pass out of the domain). The wave is excited via a vertical body forcing, centered at the $z = 0$ boundary, and the amplitude A is reduced by a factor of 10 as compared to the horizontally extended simulations (see Table 1). The low amplitude reduces any strong nonlinear effects that may arise in a constrained domain due to the continued influence of a single wave mode. The forcing for the periodic boundary simulations is specified by

$$F_z(x,z,t) = Ae^{-0.5((z-z_c)^2/\sigma_z^2)} \cdot e^{-(t-t_c)^2/2\sigma_t^2} \cos(\omega(t-t_c) - k(x-x_c)) \quad (1)$$

Table 1. Source Parameters for the Horizontally Extended Simulations

A	Source One 1×10^{-4}	Source Two 1×10^{-4}	Source Three 1×10^{-4}
τ (min)	7.5	17	6.7
t_c (min)	30	68	26.8
σ_t (min)	7.5	17	6.7
x_c (km)	0	0	0
σ_x (km)	18	40	25
z_c (km)	0	0	0
σ_z (km)	3	3	3

For the horizontally extended simulations, the numerical domain was specified to be 2000 km × 300 km with a resolution of 0.5 km in both horizontal and vertical directions. Frames were output every 60 s with a typical entire simulation length of 600 min. The bottom boundary was set to be closed and reflective; the sides and the top were specified

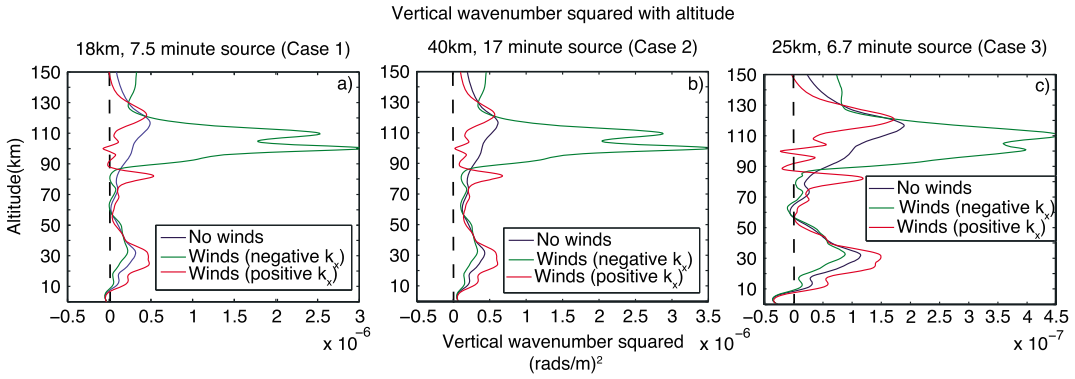

Figure 3. The predicted vertical wavelength squared plots for (a) the 18 km, 7.5 min source, (b) the 40 km, 17 min source, and (c) the 25 km, 6.7 min source.

as open boundaries. A vertical body forcing was applied which is centered at the bottom boundary and given by

$$F_z(x,z,t) = Ae^{-0.5((x-x_c)^2/\sigma_x^2+(z-z_c)^2/\sigma_z^2)} \cdot e^{-(t-t_c)^2/2\sigma_t^2} \cos(\omega(t-t_c)) \cos(k(x-x_c)) \quad (2)$$

The exact parameters used are specified in Table 1. The effect of multiplying $\cos(\omega(t - t_c)) \cos(k(x - x_c))$ is that a wave is launched in both directions, enabling us to analyze the effect of both wind/propagation directions in one simulation for the extended domain cases. For ease of analysis, two separate simulations were run in the case of the periodic simulations, one for a positive k and one for negative k. The amplitude A was deliberately specified as small to ensure that the waves remain mostly linear and interact in a linear manner; the waves in the extended domain have amplitudes in the MLT ~0.1 m/s when not scaled by density. In both the horizontally extended and periodic simulations, the wave packets were centered around (1) $\tau = 7.5$ min period and $\lambda_x = 18$ km, (2) $\tau = 17$ min period and $\lambda_x = 40$ km, and (3) $\tau = 6.7$ min period and $\lambda_x = 25$ km horizontal wavelength. Both the periodic and horizontally extended domain results are presented in terms of the density-scaled horizontal wind velocities: $u_{\text{scaled}} = u \cdot \left(\frac{\rho(z)}{\rho(z_0)}\right)^{\frac{1}{2}}$. Otherwise, waves in the upper atmosphere will dominate the plots and lower atmosphere waves will not be visible within the dynamic range.

2.4. Theory

Gravity waves can only propagate in regions of the atmosphere where their vertical wave number squared (m^2) is a positive value. A traveling wave solution turns into an exponentially decaying "evanescent" solution when its m^2 is negative. Reflection begins at a boundary where m^2 changes from positive to negative. The wave number is governed by the dispersion relation, which in its anelastic form is given by the expression [*Gossard and Hooke*, 1975]

$$m^2 = \frac{k^2N^2}{(\omega - u_0k)^2} + \frac{u_0''}{(c-u_0)} - \frac{1}{H}\frac{u_0'}{(c-u_0)} - k^2 - \frac{1}{4H^2} \quad (3)$$

where k is the horizontal wave number, ω is the ground relative frequency, u_0 is the background wind (u_0' and u_0'' are its first and second derivatives with respect to altitude), N is the buoyancy frequency, and H is the scale height. If a region of wave propagation ($m^2 > 0$) is bounded above and below by two regions of evanescence ($m^2 < 0$), then a wave can be ducted. This generally occurs due to thermal gradients (thermal ducting) or when the background wind shifts a wave's intrinsic frequency to the local buoyancy frequency (Doppler ducting) at two distinct altitudes. Strong ducting occurs approximately when an integer number of half vertical wavelength fits within the ducts vertical extent [*Walterscheid et al.*, 2001]. In this case, waves can travel vast horizontal distances with only minimal attenuation. However, if weak ducting occurs, wave energy can leak out of a duct and continue propagating into the thermosphere where it will dissipate. In addition, a wave can exhibit deep ducting in which it is trapped between some reflection height and the tropopause or ground; numerical simulations suggest that a wave can propagate over long distances via this method as well [*Walterscheid et al.*, 1999; *Yu and Hickey*, 2007b; *Snively et al.*, 2013].

We use the dispersion relation (equation (3)) to calculate the m^2 value as a function of altitude under three circumstances: no winds, wave propagation in the positive direction (positive k value), and wave propagation in the negative direction (negative k value), where the directions are specified in Figure 1. For case (1) (Figure 3a), i.e., the most commonly observed wave parameters in *Nielsen et al.* [2009], there are a number of potential ducting regions which could support long-range horizontal propagation. Even with no winds present, the thermal structure creates ducts between ~10 and 55 km altitude and a turning (reflection) point at 200 km (this is beyond the upper limit of this plot but can be seen explicitly in Figure 8a later). For a wave propagating in the positive direction, potential weak ducting regions lie between 10–55 km altitude and 92–98 km altitude. For a wave propagating in the negative direction, potential ducts are created between 10–60 km altitude and 65–80 km altitude. Notably, these results suggest that the waves should be freely propagating at the center of the OH airglow layer (87 km) for propagation in both directions.

For a wave of 17 min period, thermal or Doppler ducting is very unlikely unless there is a strong wind opposing the wave propagation direction. The average meridional winds are relatively weak, as is suggested by *Nielsen et al.* [2009, 2012]; as noted in *Snively et al.* [2013], the thermal structure is likely to play a dominant role in any reflection or ducting. At OH airglow heights (80–90 km) [e.g., *Sivjee*, 1992], waves propagating with the wind will be subject to a reduction in vertical wavelength, making the wave far more susceptible to dissipation than those traveling into the wind. If the wind is strong enough, the vertical wavelength may decrease sufficiently to produce an OH brightness response too weak to detect effectively using airglow imagers [e.g., *Gardner and Taylor*, 1998]. Thus, it may be difficult to observe waves propagating in the same direction as the MLT winds.

Figure 3c shows the predicted vertical wavelengths for case (3). The are two distinct ducts for the positive case (10–55 km altitude and 92–98 km altitude), while for the negative case there is a strong stratospheric duct above which the wave should be freely propagating.

3. Periodic Domain Results

We begin by considering the simplest case of wave propagation in a periodic domain. Periodic domains are less physical, due to the forced containment and interaction of upgoing and downgoing wave components; however, they present the opportunity to study the temporal evolution of the waves, allowing easier implementation of diagnostics. Since the periodic simulation forces exactly one horizontal wavelength into the domain, any averaging over a horizontal wavelength corresponds to simply taking an average over the x coordinate for each altitude. It also allows for isolation of a single horizontal wave mode in the Fourier domain, thus simplifying spectral analysis.

For each simulation, we take a vertical slice at $x = \lambda_x/2$ at each time step and then place the slices adjacently in an image to show the temporal evolution of both the horizontal and vertical winds. This is done for both a negative and positive wave propagation direction. In addition, we window the simulation into two halves in time and take the Fourier transform of each time series at each altitude. This gives a plot of the dominant frequency with altitude, for the first and second halves of the simulation. Therefore, we can assess which frequencies are dissipated in the first half of the simulation and which are left behind in the ducts at late times and are thus more likely to be seen at large horizontal distances from the source.

Figure 4 shows the plots described above for case (1). One thing to note is that the vertical wind strength is an important parameter in determining observable airglow perturbations as suggested by *Snively et al.* [2010]. Strong enhancements of the vertical wind are seen to occur when the wave undergoes reflection. This is because the vertical wavelength tends towards very large values as it reflects and thus more of the wave energy is associated with the vertical wind motions than the horizontal wind.

The trapping of waves between the altitudes of 10 km and 60 km is very clear in the negative propagation case, with a very regular pattern and enhancements in the vertical wind speed each time a reflection occurs at either 10 km or 60 km altitude (indicating the duct boundaries). When a reflection occurs at 60 km altitude, there is an associated transfer of wave energy into the mesosphere and thermosphere, where it dissipates. This pattern of energy transfer into the thermosphere is regular and may continue for as long as the wave is trapped in the stratosphere. The positive traveling wave shows a far more complex pattern, since reflections are far weaker than for the negative traveling case. There is certainly some trapping of the wave between 10 and 60 km, but it is much less coherent. The wave appears to be in a very small scale standing

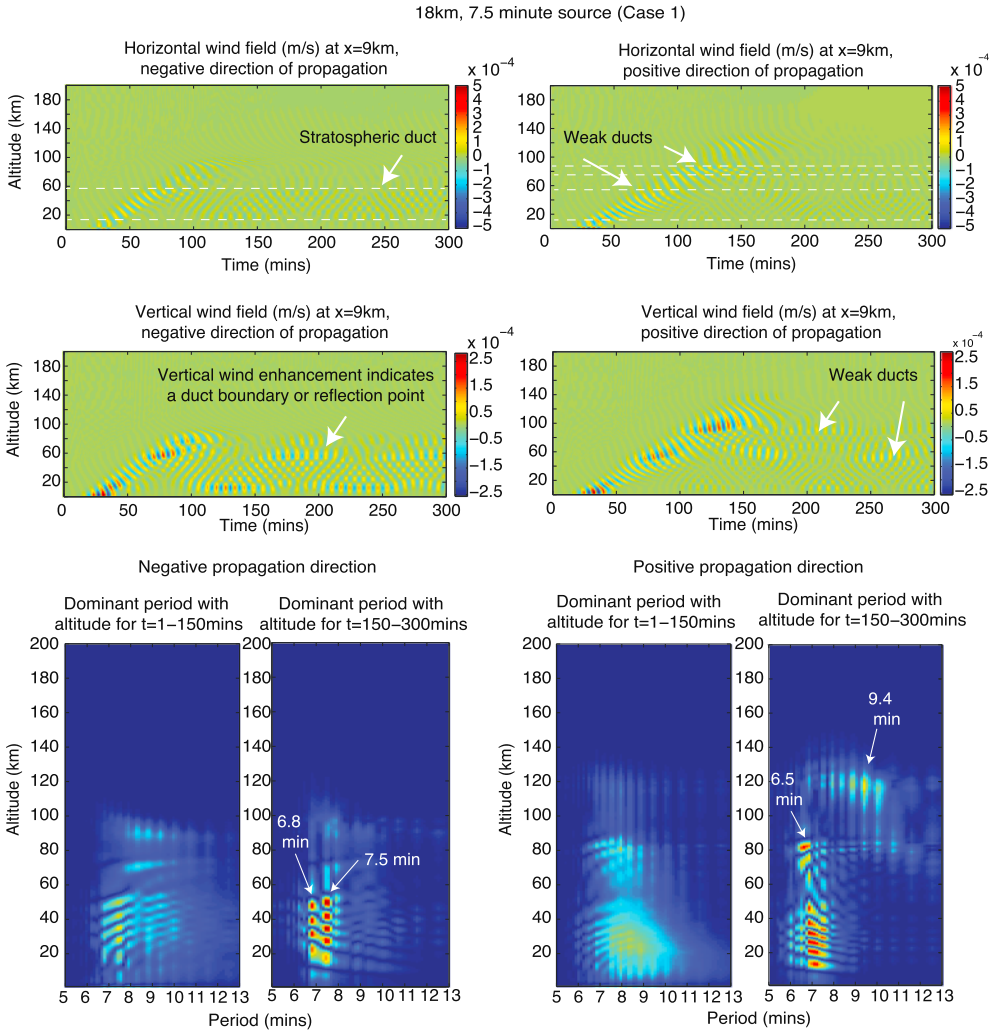

Figure 4. The temporal evolution of the horizontal and vertical winds for the 18 km, 7.5 min forcing propagating in the (left) negative direction and (right) positive direction. The bottom figures show the dominant period with altitude for the first and second half of the simulations.

wave pattern at ~ 80 km altitude (more obvious in the horizontal wind plot), above which is an enhancement in the vertical wind velocity. This vertical wind enhancement just above 80 km altitude may suggest that the positive wave is more likely to be observed in the airglow imagers. Certainly, there is more wave energy present between 80 and 100 km than in the negative case.

In the bottom half of Figure 4, we see that the negative traveling wave has a much more discrete spectrum than the positive traveling case. Over the first half of the simulation, the spectrum is much more spread over the excited range of periods; however, this forms into a more discrete pattern in the second half, when much of the initial spectrum has been dissipated or trapped within ducts. In the first half of the negative traveling wave, the long-period portion (8.82–9.37 min) of the spectra dominates at higher altitudes (specifically 75 and 90 km), while the short periods become trapped below 60 km (peaking at 7.5 min). In the second half of the simulation, most of the longer periods at high altitude are attenuated and the dominance has moved to a shorter period of 7.5 min (between ~ 55 and 75 km). Within the stratospheric duct, two dominant modes have formed at 7.5 and 6.8 min. For the positive traveling case, an initially broad spectrum (6.5–9.37 min) concentrated predominately between 10–55 km and 65–95 km is present. In the second half of the simulation, the whole distribution shifts to shorter periods and once again become more discrete in nature. In the stratospheric duct, the spectral energy is spread over ~ 6.5–7.8 min, at 80 km the spectral energy is concentrated at 6.5 min, then at 120 km the longer periods are dominant (7.5–9.37 min). It is clear that the

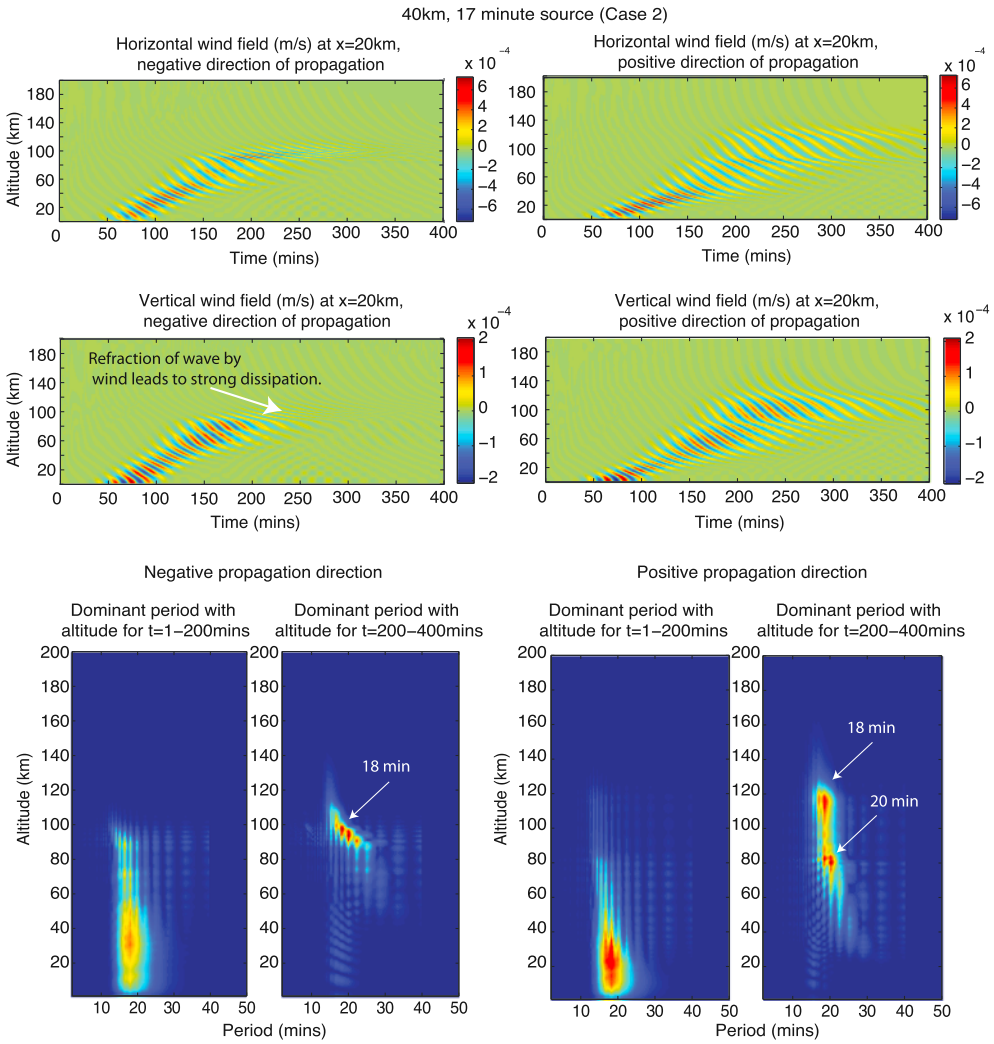

Figure 5. The temporal evolution of the horizontal and vertical winds for the 40 km, 17 min source propagating in the (left) negative direction and (right) positive direction. The bottom figures show the dominant period with altitude for the first and second half of the simulations.

short-period portion of the spectra remains trapped in the stratosphere, while the longer periods propagate into the MLT and dissipate during the earlier stages of the simulation. It is the shorter-period portion of the spectrum which will travel large horizontal distances and eventually leak into the mesosphere.

Figure 5 shows the same as the previous figure but for case (2). The negative traveling wave persists for ~150 min only, with the vertical wind speed very weak after 200 min. In fact, in the airglow layers, the wave may only be present for 50 min or so at any considerable amplitude. This provides a classic example of wave filtering in which the negative direction of propagation is subject to near-critical level filtering, whereas waves propagating in the positive direction are free to propagate with little hindrance.

From the period plots in Figure 5 (bottom), it becomes clear that only a small fraction of the waves' energy remains in the lower portion of the atmosphere in the second half of the simulation. For the negative propagating waves, the energy collects over a narrow altitude range of 90–110 km and concentrates at 18–20 min period, while the shorter-period components dominate below 55 km (14–18 min). The energy is much more spread out over a range of altitudes for the positive traveling wave, and significant enhancements are present at 80 km (20 min period) and 120 km (18.18 min period) during the second half of the simulation. Once again, the portion of the spectrum that remains at the lower altitudes is the shorter-period component (13–18 min). The shorter periods are those that become trapped within the stratosphere; it is these waves which tend to travel the largest horizontal distances.

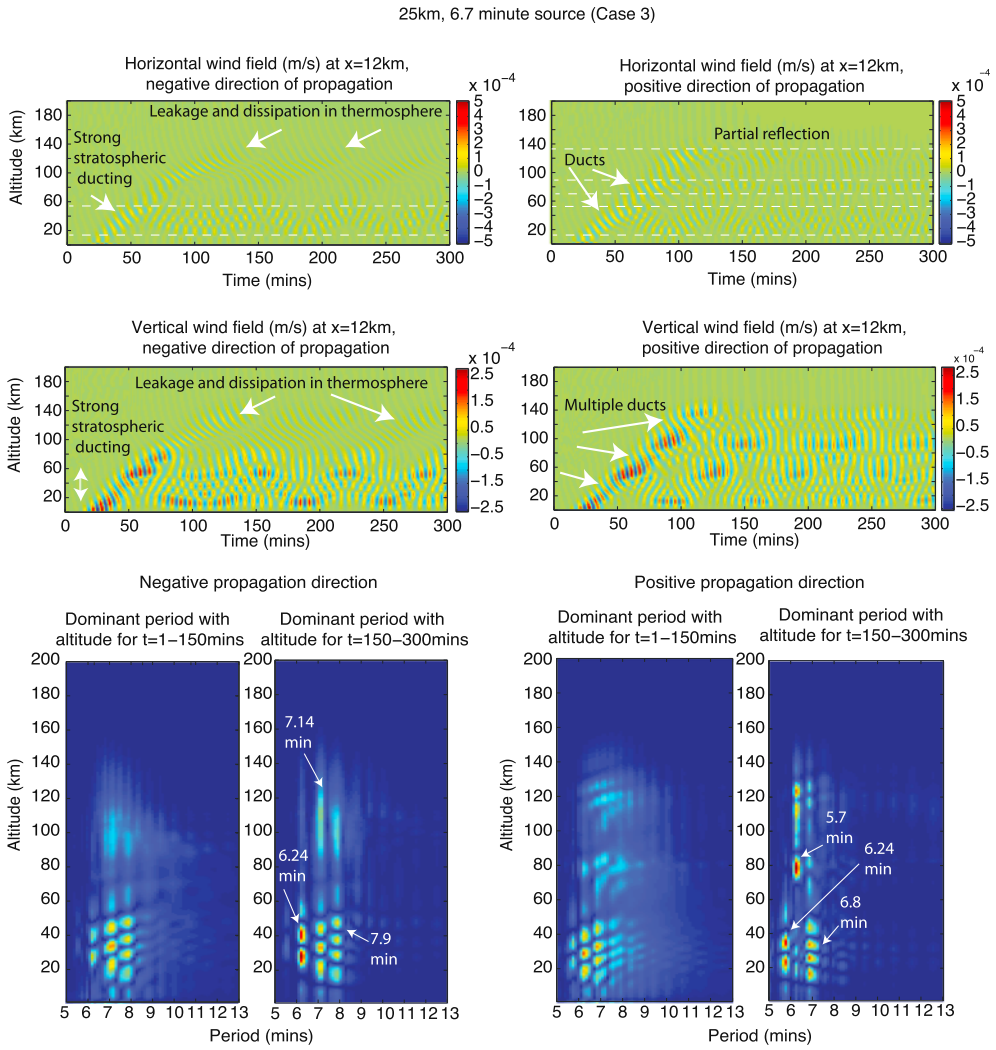

Figure 6. The temporal evolution of the horizontal and vertical winds for the 25 km, 6.7 min source propagating in the (left) negative direction and (right) positive direction. The bottom figures show the dominant period with altitude for the first and second half of the simulations.

Finally, Figure 6 shows the periodic simulations and frequency spectra for case (3). The structure of the time evolution after 150 min has a strong periodicity of about ~100 min in which the wave bounces between 60 km and 10 km while transmitting a portion of the wave following each bounce, which then propagates freely into the thermosphere where it dissipates. For the positive traveling wave, we see multiple layers of reflection, evident by the enhanced vertical wind velocity. Here the wave energy is transferred between three regions of the atmosphere, and the interference caused by wave reflection between them causes a less obvious period structure in time. The layers of propagation occur between 10–60 km, 80–90 km, and 110–130 km, and the amplitude modulates but does not decay significantly, between 150 and 300 min.

When looking at the period plots for the negative traveling wave, the spectrum does not change significantly between the first and second halves of the simulation. There are three main modes present at 6.24, 7.14, and 7.89 min, with dominance moving from 7.14 min in the first half to 6.24 min in the second half. At airglow heights, it is the 7.14 min mode which remains dominant throughout the simulation and is present over an 85–125 km altitude range. For the positive traveling wave, we see a more evenly spread spectrum in the first half, with two modes particularly dominant in the stratosphere at 6.24 and 6.81 min; in the MLT we see two more distinct altitude ranges with noticeable spectra power at ~75–85 km and 110–130 km. For the second half of the simulation, the spectrum shows more discrete modes; the 6.24 min mode is now

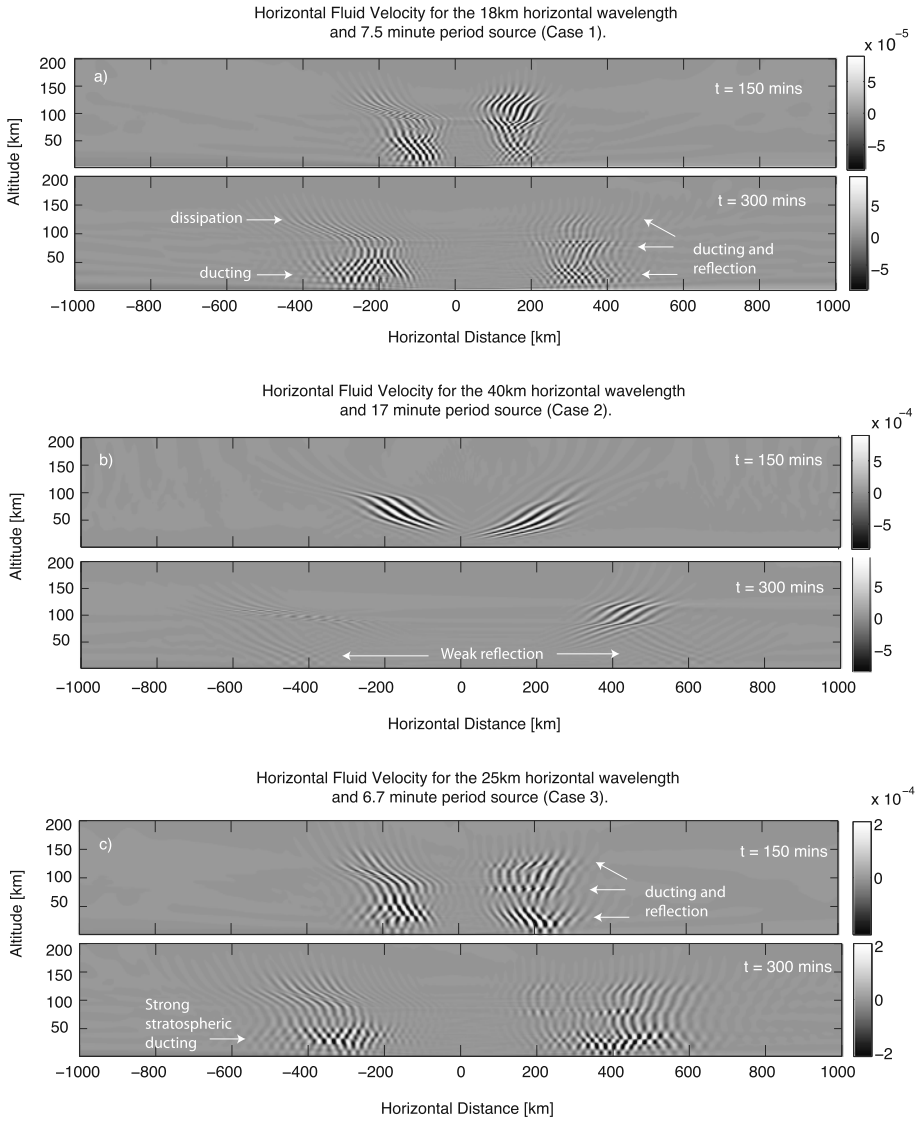

Figure 7. The horizontal wind speed at t = 150 and 300 min for (a) the 18 km, 7.5 min source; (b) the 40 km, 17 min source; and (c) the 25 km, 6.7 min source.

depleted in the stratosphere and becomes dominant in the MLT, while two modes at 6.81 and 5.76 min become dominant below 60 km.

4. Horizontally Extended Domain Results

In this section, we utilize a large 2-D grid and consider the effects of horizontal dispersion and dissipation of waves. This allows us to study their long-distance propagation in addition to their evolution in the time domain as we did with the periodic domain simulations.

4.1. Time-Dependent Results

Figure 7 shows the horizontal wind plotted at two different times for each of the three simulations. The waves are composed of a right (positive propagation direction) and left (negative propagation direction) going components in order to assess differing propagation directions relative to the wind.

In case (1) (Figure 7a), we see that a large fraction of the wave energy makes it through the ducting regions with only partial reflection and dissipates in the thermosphere. The remainder appears to be trapped predominately below 60 km and "bounces" between 10 and 60 km while dispersing horizontally as time progresses. Above 90 km, the negative propagating wave is shifted to small vertical wavelengths by the

wind which enhances dissipation. By t = 300 min, this region of dissipation spans ~ 200 km horizontally. The wave traveling in the positive direction has two evanescent regions above and below a narrow region of propagation centered at ~90 km (see Figure 3a also). Energy is transferred from the lower 10–60 km duct, tunnels through the region of evanescence above, and enters the narrow region of propagation at 90 km altitude. The wave then tunnels onto a second region of propagation above ~120 km where the wave is, once again, dissipated. Regions of horizontal wave amplitude enhancement and depletion can be seen due to the interactions between upgoing and downgoing waves as they tunnel between the stratosphere, mesosphere, and thermosphere.

For case (2) shown in Figure 7b, we see that the wave propagating in the negative direction is shifted to lower frequencies by the MLT winds, which decreases the vertical wavelength and increases the dissipation rate. Thus, at late times, it spans only a relatively narrow altitude range (~80–110 km) but is spread over a larger horizontal region than the positive traveling wave. In contrast, the wave propagating in the positive direction retains a greater amplitude, propagates higher, and spans a greater vertical portion of the atmosphere over the course of the simulation. It appears that it would be more likely to observe the positive traveling wave at airglow heights than the negative traveling wave, due to its larger amplitude and vertical wavelength. However, neither of these waves are likely to travel great horizontal distances (relative to the waves' horizontal scale) from their source, with each propagating only ~400–500 km horizontally before dissipation becomes significant. There is some partial reflection occurring (indicated on plot), but it is weak compared to the transmitted amplitudes. Due to the relatively low frequency of the wave, it is not subject to ducting unless very strong winds are present in the mesosphere, in which case, reflection and deep ducting could occur for waves traveling against the background flow. Thus, conditions for long-range propagation of this wave are poor, and an imager would likely have to be near the source region itself to observe the primary signature of these waves.

For case (3) in Figure 7c, the negative traveling wave freely propagates upward and dissipates at ~150 km altitude. The positive traveling wave has a ducted pattern emerging at ~100 km and ~120 km. By 300 min, it is clear that there are three distinct regions of propagation in the positive traveling case (stratosphere, upper mesosphere, and lower thermosphere), whereas there is only strong ducting within the stratosphere for the negative traveling case. In both cases, the wave disperses significantly in the stratosphere, and by t = 300 mins, the wave spans ~ 400 km in this region without significant dissipation.

4.2. Kinetic Energy Density Results

In order to better assess potential ducting regions, at each grid point we calculate the time-averaged kinetic energy density at each grid point (over 600 min) and plot the log of this value in Figure 8. The kinetic energy density is given by

$$\text{K.E.} = \frac{1}{2}\rho(u'^2 + w'^2) \tag{4}$$

where ρ is the background density and u' and w' are the horizontal and vertical perturbation velocities. This gives an indication of where the wave energy density is most likely to reside and takes into account both the horizontal and vertical winds. Note, however, that this presentation is dependent on the duration of the simulation; if it were run for longer, the energy density distribution would extend further horizontally and the vertical distribution could differ as more energy leaks out of the stratosphere. The calculated vertical wave number squared plots are overlaid on top with the center being zero vertical wave number and the green line corresponding to a negative propagation direction and the red corresponding to positive. Note that this shows the shape of the profile only and is intended for qualitative identification of regions of evanescence and ducting; the axis or values are not displayed.

For case (1), shown in Figure 8a, the wave propagating in the negative direction, the trapping of wave energy density between ~10 and 60 km, is very apparent. Between 60–70 and 80–87 km, the wave energy is slightly diminished, suggesting that the wave is not subject to trapping here, while in between 75 km is a region of increased energy density. The overlaid predicted vertical wavelength plot (green line for negative propagation) shows that the relative energy density increase at 75 km altitude coincides with a stable region caused by a small positive wind peak at 80 km (see Figure 1). The horizontally periodic nature of the energy density suggests that it is being fed from the stratospheric duct below. This highlights the importance of the stratosphere for containing waves that may travel over long distances. For the wave propagating in the positive direction, the majority of the wave energy density propagates upward into the mesosphere, with a

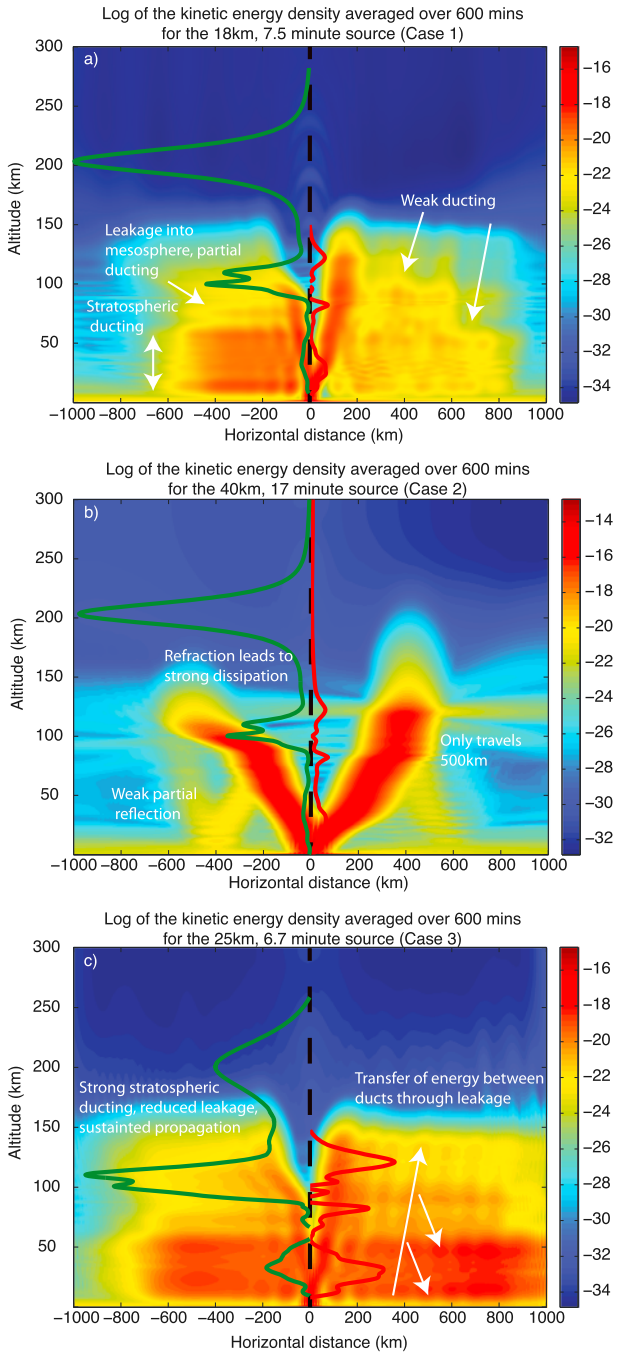

Figure 8. The log of the time-averaged kinetic energy density averaged at each grid point over the duration of the simulation for the (a) 18 km, 7.5 min source, (b) 40 km, 17 min source, and (c) 25 km, 6.7 min source. Overlaid are the vertical wavelength squared calculations with green indicating negative propagation and red indicating positive propagation. Note that the black line in the center indicates zero vertical wave number.

much weaker reflection at 60 km. There is evidence for reduced energy density regions between 82–89 and 100–120 km, which surround a relatively strong region of energy density at 90 km altitude caused by a small mesospheric wind inversion at this height. The lack of potential ducts, as shown in the vertical wave number plot (red line), hinders the ability of the wave to become trapped and to effectively travel over large horizontal distances. Once again, the energy density at 90 km appears to be fed by the upward leakage of energy density from the weak stratospheric duct. Due to the stronger reflection/wave trapping below 60 km, the wave propagating in the negative direction is most likely to travel the largest horizontal distance. However, the kinetic energy density is more likely to be trapped in the airglow region for the positive wave and may produce a more observable if less horizontally continuous response in OH intensity. In reality, the waves observed by airglow imagers in this region, for both propagation directions, would probably be freely propagating waves as suggested in *Nielsen et al.* [2012]. Many of these observed waves are likely to have leaked from the stratosphere over time.

For case (2), shown in Figure 8b, we can see that a major fraction of the wave energy simply propagates into the thermosphere and dissipates. The positive traveling waves are able to reach higher into the atmosphere due to their propagation against the prevailing wind at MLT heights. Weak reflection occurs in both cases; however, it is not a significant portion of the wave's energy density. It also appears that secondary waves are excited by the dissipation of the wave traveling in the positive direction.

For case (3), shown in Figure 8c, the stratospheric ducting is stronger for the wave propagating in the negative direction due to the evanescent region between ~55 and 65 km, and the kinetic energy density is smoothed into two distinct peaks (10 km and 60 km) at large horizontal distances, due to dispersion of the trapped wave modes. Above 100 km altitude, the wave becomes subject to dissipation as the wind Doppler shifts the wave to smaller vertical scales, but the dissipation is not as strong as for the longer-period wave in case (2). The amount of energy density transmitted to the thermosphere decreases with increasing distance from the

source. This is because the longer-wave periods (such as case (3)) only undergo weak reflection at 60 km and dissipate in close horizontal proximity to the source region. However, as time and horizontal distance from the source increases, the periods which remain are those that are well trapped within the stratosphere; thus, only a small amount of leakage occurs. For the wave traveling in the positive direction, there is a much more noticeable horizontally periodic structure in the stratospheric region when compared to the negative traveling wave. This is a consequence of a less effective and more leaky duct, leading to periodic transfer of energy density between the stratospheric ducting region and a second potential ducting region at ~90 km, in which the vertical wave number plot (Figure 3) shows a narrow region of propagation surrounded by two narrow evanescent regions. There is also the potential for reflection at ~ 150 km for any waves which have not dissipated before they reaches this altitude.

Interestingly, results from Figure 2 suggest that there would be a strong enhancement in kinetic energy at 87 km (when averaged over ± 8 km) for the negative traveling wave as opposed to the positive traveling wave. This highlights a potential difference between using a 1-D steady state approach, in which energy is constantly added to the system, and a 2-D wave packet approach. It is likely due to the rapid ascent and dissipation of the waves: At 87 km the wave is mostly freely propagating and has an angle of propagation ($\vec{k} = k\hat{x} + m\hat{z}$) which is close to optimum for both horizontal and vertical perturbation velocities (i.e., 45°) and suggests large group velocity as the wave tunnels out of the stratosphere. If a wave was continually forced (as it is in *Snively et al.* [2013] and Figure 2), then there would be an appearance of enhancement in the kinetic energy.

Another subtle effect is that strong duct regions in the mesosphere do not necessarily guarantee successful long-range (and long-duration) propagation. A region of high stability bounded by two evanescent regions can create a very good duct if its vertical extent is equal to a half integer multiple of the vertical wavelength of the wave. However, regions of strong stability in the MLT decrease the wave's vertical scale and make it more susceptible to dissipation or breaking at high altitudes. This implies that waves may travel farther in a stratospheric duct, where dissipation caused by molecular viscosity and thermal conduction is relatively unimportant, than they would in a mesospheric duct. If the stratospheric duct is too effective, however, then relatively little energy will leak into the mesosphere each time the wave reflects at the upper duct boundary, and as a result the energy will be spread over a larger horizontal distance.

5. Momentum Flux and Body Forcing Effects

In order to look at the momentum carried and deposited by the gravity waves, we investigate the vertical flux of horizontal momentum and its vertical derivative [e.g., *Gardner et al.*, 1999; *Swenson et al.*, 1999; *Nappo*, 2002; *Zhang and Yi*, 2002; *Vadas and Fritts*, 2005; *Vadas*, 2007; *Yigit et al.*, 2008; *Liu et al.*, 2013]. Previous studies have only considered the dissipation of an upward propagating packet that does not experience significant reflection or ducting; here we consider in particular waves that are subject to reflection.

The vertical flux of horizontal momentum is given by $\rho_0\overline{u_1 w_1}$, and the vertical derivative $-\frac{1}{\rho_0}\frac{\partial \rho_0 \overline{u_1 w_1}}{\partial z}$ can be interpreted as the associated body forcing due to changes in momentum flux, which acts to accelerate or decelerate the background wind [e.g., *Vincent and Reid*, 1983; *Vadas and Fritts*, 2005; *Vadas*, 2007; *Liu et al.*, 2013]. Here ρ_0 is the background density, u_1 and w_1 are the horizontal and vertical perturbation velocities, respectively, and the overline denotes a horizontal average. Most previous modeling studies use periodic domains to assess momentum and energy flux [e.g., *Zhang and Yi*, 2002; *Yu and Hickey*, 2007b; *Liu et al.*, 2013]. This type of domain horizontally confines the wave and enforces that upward and downward propagating wave components will interact with each other, an effect which becomes enhanced in a duct. In reality, waves propagate horizontally and are able to disperse, leading to a more complex and highly time-dependent superposition (and, at larger amplitudes, interaction) between upgoing and reflected wave modes.

From linear theory and under the assumption that $\omega >> f$, the momentum flux (per unit mass) can be written as $-\frac{m}{k}\overline{w^2}$ by using the polarization relations. We note the argument in *Fritts* [2000] that when reflecting, the vertical wave number m goes to zero (vertical wavelength tends to infinity) and thus the momentum flux of a gravity wave also goes to zero. The reflected wave then propagates in the opposing vertical direction, and the momentum flux carries a negative sign relative to the transmitted wave. This is also true of the energy flux $\overline{p_1 w_1}$ as seen in *Yu and Hickey* [2007b]. Following this argument, the change in momentum flux that occurs as it reflects could be construed $\left(\text{via} -\frac{1}{\rho_0}\frac{\partial \rho_0 \overline{u_1 w_1}}{\partial z}\right)$ as a "body force." However, the reflection of

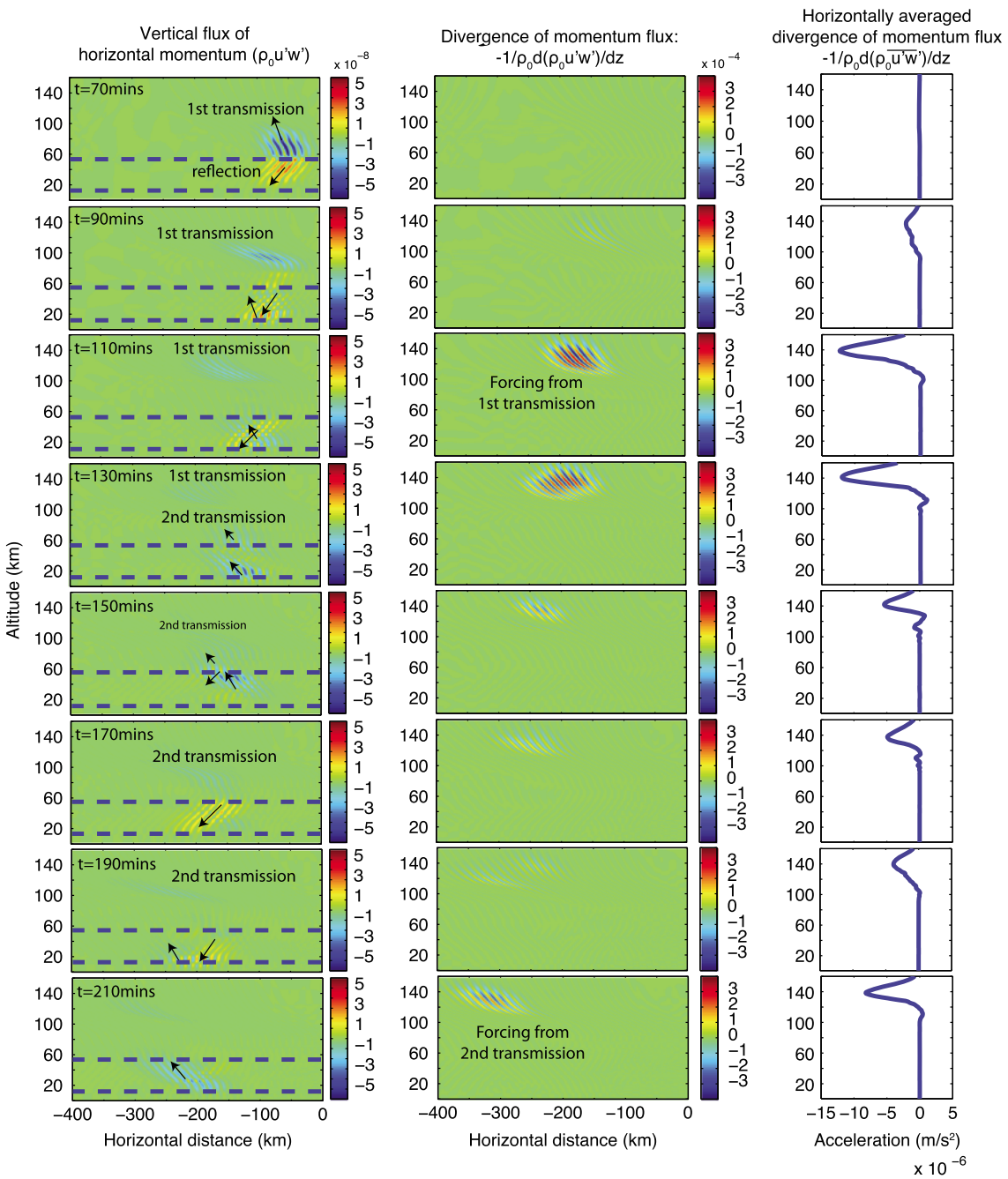

Figure 9. The vertical flux of horizontal momentum and its associated divergence. Shown for the negative propagation direction of the 25 km, 6.7 min source (case (3)).

the wave does not strictly contribute to the acceleration or deceleration of the background wind. Therefore, care must be taken in interpreting the results of such an analysis.

It is commonly assumed that ducted waves do not contribute to the vertical flux of horizontal momentum. A perfectly ducted wave will have no net vertical propagation due to superposition of upward and downward components and will experience predominantly horizontal propagation. However, in reality, waves are not perfectly ducted, and leakage from the boundaries of a duct can release propagating waves that can dissipate and contribute to an overall net momentum flux and forcing of the MLT.

To highlight this effect, we plot the momentum flux and the associated "body forcing" for the negative direction of propagation case (3), in Figure 9. As previously mentioned, a fraction of the wave spectrum is ducted

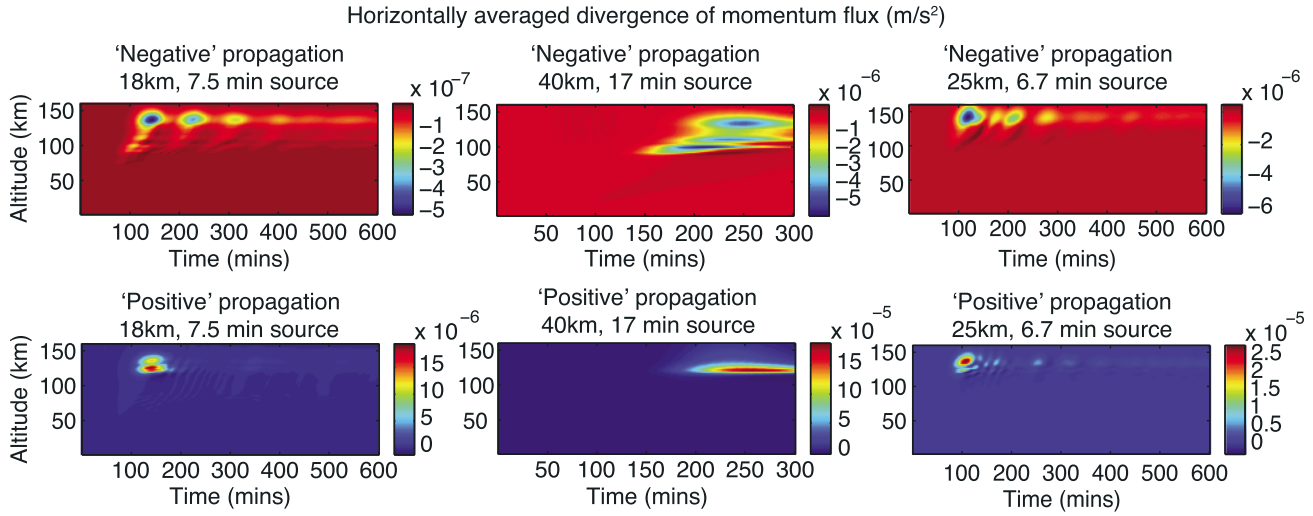

Figure 10. The horizontally domain averaged divergence of momentum flux (body forcing per unit mass, in units of m s^{-2}) for each of the three sources split into the negative and positive propagating portions of the simulation.

in the stratosphere and travels predominantly horizontally as it reflects between ~10 and 60 km. Each time the wave reflects off the upper duct boundary at 60 km altitude, it transmits a portion of its energy, which propagates freely in the thermosphere and dissipates, producing a body forcing on the background wind. Over time, the wave packet disperses and different parts of the packet reflect off the 60 km duct boundary at different times. The stratospheric ducted wave acts like a moving source of thermospheric wave energy and momentum, which it supplies periodically over distance as the wave disperses and dissipates. It is clear that ducted waves can contribute to a periodic forcing of the thermosphere, which could potentially extend over mesoscale distances (~ 1000 km).

Figure 10 compares the time-dependent body forcings (per unit mass), horizontally averaged over the entire domain for the negative and positive propagation directions in each case. Although we lose the spatial distribution of the forcing, we gain an insight into the time dependence of the thermospheric forcing by doing this. There is a clear anisotropy between the forcing in the negative and positive propagation directions, noting that the former decelerates the background wind while the latter accelerates it. The positive direction of propagation always has approximately an order of magnitude greater peak forcing than its negative propagating counterpart. This is partly due to a greater fraction of energy and momentum being trapped at lower altitudes in the case of the negative propagation direction and partly due to the distribution of momentum over altitude.

In three cases (negative and positive propagation in the 25 km, 6.7 min forcing and negative propagation in the 18 km 7.5 min forcing), we see a periodic forcing structure in the thermosphere, the most consistent of which is the negative propagating wave in the 18 km 7.5 min forcing case. The first peak forcing has a value of -5.05×10^{-7} m/s^2 (however, since we did not base our initial wave amplitude upon realistic values, we are more concerned with the available distribution of flux and its relative decrease) and occurs 146 min into the simulation at an altitude of 136 km. The next three successive maxima have amplitudes of 71%, 40%, and 26% of the first maxima respectively. In comparison, the negative propagating wave in the 25 km, 6.7 min forcing case has second and third maxima at 50% and 31% of the first maxima respectively. Interestingly, there is a double maxima at two different altitudes (~ 10 km apart) which occurs for positive propagation in the 25 km and 18 km forcing cases. This appears to be due to interference between dissipating upward traveling waves and reflection from the turning point at ~ 140 km (as shown in Figure 3). This highlights the fact that reflection in the thermosphere and "deep ducting" (when a wave is trapped over a broad range of altitudes) can prevent dissipation and local body forcing, in addition to contributing to extended wave propagation. While our amplitudes are deliberately chosen to be small to avoid nonlinearities, *Vadas and Liu* [2009] assess the body forcing associated with gravity waves generated from a convective plume using ray trace simulations and suggest a maximum forcing of ~1.3 m/s^2. *Liu et al.* [2013] used 2-D numerical

simulations to estimate that the nondensity-scaled momentum flux ($\overline{u'w'}$) is of the order of 10^{-3} m^2/s^2 in the mesosphere, for waves of an initial density-scaled amplitude of 1×10^{-3} m/s launched at 60 km. These studies investigated the dissipation of upward propagating waves and did not consider the reflection and ducting of the waves, which we have focused upon.

6. Discussion

In this paper, we simulated the propagation of three different wave spectra under diurnally averaged background winds and high-latitude conditions. Simulations were run to compare propagation into and against the background meridional wind and were inspired by the climatologies discussed in *Nielsen et al.* [2009, 2012] and complementary modeling by *Snively et al.* [2013]. We have investigated the directionality of propagation and the specified forcing parameter effects on the ability for a wave packet to propagate over large horizontal distances.

Using a combination of periodic domain and horizontally extended simulations, we studied (1) an 18 km, 7.5 min forcing based upon the average wave characteristics seen in *Nielsen et al.* [2009]; (2) a 40 km, 17 min period forcing which has average phase speed observed but outlying wavelength and periods; and (3) a 25 km, 6.7 min forcing chosen from *Snively et al.* [2013] which was suggested to have strong ducting characteristics.

The meridional winds at high latitudes are relatively weak, and there is an absence of strong jets. The maximum wind speed below 150 km (where most waves are present) is only 27 m/s; thus, the thermal structure will dominate wave reflection and refraction. However, the winds must not be discounted and certainly have some effect on wave propagation. Throughout the paper, we consider diurnally averaged meridional winds at one location; however, accounting for the variability of the winds in both time and position can be significant. Below 50 km, where the majority of wave trapping was seen to occur, the winds do not exhibit a great deal of variability. Therefore, the facilitation of long-range propagation via this method may remain valid; however, the variability and direction of the winds in the MLT can be dependent on both seasonal and geographical factors [e.g., *Sharma et al.*, 2010; *Day et al.*, 2012; *Day and Mitchell*, 2013]. Also, the effect of time dependence of background winds on small-scale waves is currently not well understood or constrained; however, ray trace studies have suggested that time dependence of winds can facilitate upward propagation and reduce critical levels [e.g., *Broutman and Young*, 1986; *Eckermann*, 1997; *Sartelet*, 2003]. The effect of this wind variability is beyond the scope of this paper, and we have attempted to capture an average scenario for comparisons with statistical studies. However, it is important to note that it could be important in modifying the propagation, reflection, and dissipation of small-scale waves, which we will address in further studies.

It is clear from both the horizontally extended and periodic domain simulations that significant wave trapping occurs in the stratosphere and that trapping in this region provides an important mechanism for facilitating long-range propagation. Due to the negligible kinematic viscosity and thermal conduction at low altitudes, waves can propagate in the stratosphere with little attenuation once trapped, a result also seen by *Yu and Hickey* [2007b]. The dominant loss mechanism from the stratospheric duct is leakage into the upper atmosphere. The wave energy is more effectively trapped between 10 and 60 km for the negative traveling waves in all three forcing conditions, and the ducting became stronger as the dominant wave period was reduced. From our simulations, it is suggested that the majority of waves seen in the MLT at large horizontal distance from the source is a result of leakage from the stratosphere or deep ducting. In such cases, waves which are more effectively trapped in the stratosphere would travel farther distances, but the wave energy leaked in the MLT per unit of horizontal distance would be less and perhaps produce weaker intensity responses in the airglow.

Typically, we saw that the negative traveling waves were more likely to be freely propagating and be subject to enhanced dissipation (due to MLT winds decreasing vertical scales) above 80 km. The strength of dissipation for those waves would increase with increasing period, while the positive traveling waves were more likely to experience reflection and partial ducting in the MLT. Without winds, the background temperature structure would allow waves to freely propagate through this region, but the inclusion of the negative winds from 90 to 110 km causes ducting and reflection for positive propagation direction and small vertical scales and increased dissipation in the negative propagation direction. From the periodic simulations, the dominant periods are shorter in the second half of the simulation when compared to the first. This is due

to lack of trapping and reflection experienced by the longer periods which dissipate relatively quickly after reaching high altitudes. In particular, the modes which get trapped in the stratosphere at late times are the higher-frequency components of the excited wave packet.

For case (3), in which very little of the wave amplitude was subject to reflections or trapping, the waves were strongly dissipated when propagating in the negative direction due to the MLT winds, while propagation was free in the positive direction. This highlights classic wave direction anisotropies as suggested in *Walterscheid et al.* [2001], and the effect is very important for waves which have long enough periods that reflection is negligible. In either direction, waves not subject to ducting or reflection will not likely travel large horizontal distances relative to their scale; hence, unless an observer is close to the source, these waves are less likely to be seen.

In terms of the periods observed for the 6.7 and 7.5 min sources, those shorter than ~ 6.8 min tended to be contained below 80 km while those longer than ~ 8 min tended to dissipate in the first half of the simulation for the 25 km, 6.7 min forcing and the 18 km 7 min forcing. For periods between 6.8 and 8 min, the mode was seen in both the stratosphere and above 80 km and was present for the entirety of the simulation. For the 40 km, 17 min forcing periods longer than 18 min were not present or weak in the second half of the simulation below 60 km, while those between 14 and 18 min were present over the entire time and altitude range but were significantly weaker.

We note that for three cases (negative and positive propagation in case (3) and negative propagation in case (1)), we see a periodic and horizontally distributed body forcing on the thermosphere, due to the vertical change in momentum flux, with the positive traveling waves producing an order of magnitude greater peak forcing than the negative traveling waves. Ducted waves are typically not considered as contributing to the net momentum flux; however, we see that this periodic forcing arises as a result of a periodic leakage from the stratospheric duct. Therefore, momentum associated with ducted waves can contribute to the net forcing of the upper atmosphere and can be distributed both horizontally and temporally. We also suggest that reflection in the thermosphere can erroneously be interpreted as a body forcing due to the momentum flux going to zero when the reflection occurs [e.g., *Fritts*, 2000]. Thus, the evolutions and effects of waves can be assessed only with insight across a wide range of altitudes and time scales.

7. Conclusions

Based on the conditions and simulations in this paper, we note three main possible scenarios: (1) Waves undergo very weak reflection and very little ducting due to long periods relative to the buoyancy period, in which case the waves will travel into the thermosphere and be subject to enhanced dissipation if propagating with the MLT wind. This case is not conducive to long-range propagation. (2) Waves are partially reflected and ducted at several different layers in the atmosphere, in this case the farthest propagation occurs in the stratosphere; however, energy is constantly being transferred between it, the mesospheric, and lower thermospheric ducts. Here waves are more likely to be seen as enhanced in the airglow region as reflection and ducting in this region cause enhancements in the vertical wind speed. This was observed here in particular for the positive traveling waves due to the wind peaks opposing the propagation direction in the mesopause and in thermosphere, with a region of stability in between. (3) A wave is trapped effectively in the stratosphere and can travel large horizontal distances with little dissipation. The potential for ducting in this region is high due to the nature of the stratospheric thermal structure; only small-magnitude winds are required to make it into an effective duct for short-period waves propagating against the flow.

It had been previously suggested [*Fritts*, 2000] that ducted waves are unlikely to contribute to forcing of the background atmosphere; however, we show that forcing can occur potentially far from the source region through duct leakage. The forcing response in the MLT can be periodic in time and distributed horizontally due to leakage from the duct, but the forcing will decrease in magnitude with each occurrence, and the supply of wave momentum and energy is depleted from the duct.

In summary, a significant fraction of waves observed at MLT altitudes may be subject to ducted propagation at lower altitude. Waves are more likely to travel over large horizontal distances when trapped in the stratosphere than they are when trapped in the MLT due to the relatively weak effect of dissipation on waves below the MLT region.

Acknowledgments
Research by C.J. Heale and J.B. Snively was supported under NSF grants AGS-1113427 and AGS-1151746. Research by M.P. Hickey was supported under NSF grant AGS-1001074. Copies of the simulation data and figures can be obtained on request to the authors.

References

Broutman, D., and W. Young (1986), On the interaction of small-scale oceanic internal waves with near-inertial waves, *J. Fluid. Mech.*, *166*, 341–358.
Chimonas, G., and C. Hines (1986), Doppler ducting of atmospheric gravity waves, *J. Geophys. Res.*, *91*(D1), 1219–1230.
Clawpack Development Team (2014), Clawpack Software, Version 4.6. [Available at http://www.clawpack.org.]
Day, K. A., and M. J. Mitchell (2013), Mean winds in the MLT, the SQBO and MSAO over Ascension Island (8°S, 14°W), *Atmos. Chem. Phys.*, *13*(18), 9515–9523.
Day, K. A., M. J. Taylor, and M. J. Mitchell (2012), Mean winds, temperatures and the 16- and 5-day planetary waves in the mesosphere and lower thermosphere over Bear Lake Observatory (42°N, 111°W), *Atmos. Chem. Phys.*, *12*(3), 1571–1585.
Drob, D. P., et al. (2008), An empirical model of the Earth's horizontal wind fields: HWM07, *J. Geophys. Res.*, *113*, A12304, doi:10.1029/2008JA013668.
Eckermann, S. D. (1997), Influence of wave propagation on the doppler spreading of atmospheric gravity waves, *J. Atmos. Sci.*, *54*, 2554–2573.
Fritts, D. C. (2000), Errant inferences of gravity wave momentum and heat fluxes using airglow and lidar instrumentation: Corrections and cautions, *J. Geophys. Res.*, *105*(D17), 22,355–22,360.
Fritts, D. C., and T. S. Lund (2011), Gravity wave influences in the thermosphere and ionosphere: Observations and recent modeling, in *Aeronomy of the Earth's Atmosphere and Ionosphere*, vol. 2, pp. 109–130, Springer, Netherlands.
Fritts, D. C., and R. Vincent (1987), Mesospheric momentum flux studies at Adelaide, Australia, *J. Atmos. Sci.*, *44*, 605–619.
Fritts, D. C., S. L. Vadas, K. Wan, and J. A. Werne (2006), Mean and variable forcing of the middle atmosphere by gravity waves, *J. Atmos. Sol. Terr. Phys.*, *68*, 247–265.
Gardner, C. S., and M. J. Taylor (1998), Observational limits for lidar, radar, and airglow imager measurements of gravity wave parameters, *J. Geophys. Res.*, *103*(D6), 6427–6437.
Gardner, C. S., Y. Z. K. Gulati, and G. R. Swenson (1999), Measuring gravity wave momentum fluxes with airglow images, *J. Geophys. Res.*, *104*, 1903–1915.
Gossard, E. E., and W. H. Hooke (1975), *Waves in the Atmosphere*, 456 pp., Elsevier, New York.
Heale, C. J., J. B. Snively, M. P. Hickey, and C. J. Ali (2014), Thermospheric dissipation of upward propagating gravity wave packets, *J. Geophys. Res. Space Physics*, *119*, 3857–3872, doi:10.1002/2013JA019387.
Hecht, J., R. L. Walterscheid, M. P. Hickey, and S. Franke (2001), Climatology and modeling of quasi-monochromatic atmospheric gravity waves observed over Urbana, Illinois, *J. Geophys. Res.*, *106*(D6), 5181–5195.
Hibbins, R. E., P. J. Espy, and M. J. Jarvis (2006), Mean winds and tides in the mesosphere and lower thermosphere above Halley, Antarctica, *J. Atmos. Sol. Terr. Phys.*, *68*(3-5), 436–444.
Hickey, M. P. (2001), Airglow variations associated with non-ideal ducting of gravity waves in the lower thermosphere region, *J. Geophys. Res.*, *106*, 17,907–17,917.
Isler, J., M. Taylor, and D. Fritts (1997), Observational evidence of wave ducting and evanescence in the mesopshere, *J. Geophys. Res.*, *102*, 26,301–26,312.
Liu, X., J. Xu, J. Yue, and S. L. Vadas (2013), Numerical modeling study of the momentum deposition of small amplitude gravity waves in the thermosphere, *Ann. Geophys.*, *31*, 1–14, doi:10.5194/angeo-31-1-2013.
Nappo, C. J. (2002), *An Introduction to Atmospheric Gravity Waves, Int. Geophy. Ser.*, vol. 85, Academic Press, San Diego, Calif.
Nielsen, K., M. Talor, R. Hibbins, and M. Jarvis (2009), Climatology of short-period mesospheric gravity waves over Halley, Antarctica (76°S, 27°W), *J. Atmos. Sol. Terr. Phys.*, *71*, 991–1000.
Nielsen, K., M. J. Taylor, R. E. Hibbins, M. J. Jarvis, and J. M. Russel III (2012), On the nature of short-period mesospheric gravity wave propagation over Halley, Antarctica, *J. Geophys. Res.*, *117*, D05124, doi:10.1029/2011JD016261.
Pautet, P., M. Talyor, A. Liu, and G. Swenson (2005), Climatology of short-period gravity waves observed over northern Australia during the Darwin Area Wave Experiment (DAWEX) and their dominant source regions, *J. Geophys. Res.*, *110*, D03S90, doi:10.1029/2004JD004954.
Picone, J. M., A. E. Hedin, D. P. Drob, and A. Aikin (2002), NRL-MSISE-00 empirical model of the atmosphere: Statisical comparisons and scientific issues, *J. Geophys. Res.*, *107*(A12), 1468, doi:10.1029/2002JA009430.
Pitteway, M. L. V., and C. O. Hines (1963), The viscous damping of atmospheric gravity waves, *Can. J. Phys.*, *41*, 1935–1948.
Sartelet, K. N. (2003), Wave propagation inside an inertial wave. Part I: Role of time dependence and scale separation, *J. Atmos. Sci.*, *60*(12), 1433–1447.
Sharma, A., M. Rokade, R. Kondala Rao, S. Gurubaran, and P. Patil (2010), Comparative study of MLT mean winds using MF radars located at 16.8°N and 8.7°N, *J. Earth Syst. Sci.*, *119*(4), 461–470.
Simkhada, D. B., J. B. Snively, M. J. Taylor, and S. J. Franke (2009), Analysis and modeling of ducted and evanescent gravity waves observed in the Hawaiian airglow, *Ann. Geophys.*, *27*, 3213–3224, doi:10.5194/angeo-27-3213-2009.
Sivjee, G. G. (1992), Airglow hydroxyl emissions, *Planet. Space Sci.*, *40*(2-3), 235–242.
Snively, J., V. Pasko, and M. Taylor (2010), OH and OI airglow layer modulation by ducted short-period gravity waves: Effects of trapping altitude, *J. Geophys. Res.*, *115*, A11311, doi:10.1029/2009JA015236.
Snively, J. B., and V. P. Pasko (2003), Breaking of thunderstorm-generated gravity waves as a source of short-period ducted waves at mesopause altitudes, *Geophys. Res. Lett.*, *30*(24), 2254, doi:10.1029/2003GL018436.
Snively, J. B., and V. P. Pasko (2008), Excitation of ducted gravity waves in the lower thermosphere by tropospheric sources, *J. Geophys. Res.*, *113*, A06303, doi:10.1029/2007JA012693.
Snively, J. B., K. Nielsen, M. P. Hickey, C. J. Heale, M. Talyor, and T. Moffat-Griffin (2013), Numerical and statistical evidence for long-range ducted gravity wave propagation over Halley, Antarctica, *Geophys. Res. Lett.*, *40*, 4813–4817, doi:10.1002/grl.50926.
Stobie, J. G., F. Einaudi, and L. W. Uccellini (1983), A case study of gravity waves—Convective storms interactions: 9 May 1979, *J. Atmos. Sci.*, *40*, 2804–2830.
Sutherland, B. R., and K. Yewchuk (2004), Internal wave tunneling, *J. Fluid Mech.*, *511*, 125–134.
Suzuki, S., K. Shiokawa, Y. Otsuka, T. Ogawa, and P. Wilkinson (2004), Statistical characteristics of gravity waves observed by an all-sky imager at Darwin, Australia, *J. Geophys. Res.*, *109*, D20S07, doi:10.1029/2003JD004336.
Suzuki, S., K. Shiokawa, Y. Otsuka, S. Karwamura, and Y. Murayama (2013), Evidence of gravity wave ducting in the mesopause region from airglow network observations, *Geophys. Res. Lett.*, *40*, 601–605, doi:10.1029/2012GL054605.
Swenson, G. R., R. Haque, W. Yang, and C. S. Gardner (1999), Momentum and energy fluxes of monochromatic gravity waves observed by an OH imager at Starfire Optical Range, New Mexico, *J. Geophys. Res.*, *104*(D6), 6067–6080.

Taylor, M. J., W. R. Pendleton Jr., S. Clark, H. Takahashi, D. Gobbi, and R. A. Goldberg (1997), Image measurements of short-period gravity waves at equatorial latitudes, *J. Geophys. Res.*, *102*(D22), 26,283–26,299.

Tuan, T., and D. Tadic (1982), A dispersion formula for analyzing "modal interference" among guided and free gravity wave modes and other phenomena in a realistic atmosphere, *J. Geophys. Res.*, *87*(A3), 1648–1668.

Vadas, S. L. (2007), Horizontal and vertical propagation and dissipation of gravity waves in the thermosphere from lower atmospheric and thermospheric sources, *J. Geophys. Res.*, *112*, A06305, doi:10.1029/2006JA011845.

Vadas, S. L., and D. C. Fritts (2005), Thermospheric responses to gravity waves: Influences of increasing viscosity and thermal diffusivity, *J. Geophys. Res.*, *110*, D15103, doi:10.1029/2004JD005574.

Vadas, S. L., and H. L. Liu (2009), Generation of large-scale gravity waves and neutral winds in the thermosphere from the dissipation of convectively generated gravity waves, *J. Geophys. Res.*, *114*, A10310, doi:10.1029/2009JA014108.

Vincent, R. A., and I. M. Reid (1983), HF Doppler measurements of mesospheric momentum fluxes, *J. Atmos. Sci.*, *40*, 1321–1333.

Walterscheid, R., and M. P. Hickey (2009), Gravity wave ducting in the upper mesosphere and lower thermosphere duct system, *J. Geophys. Res.*, *114*, D19109, doi:10.1029/2008JD011269.

Walterscheid, R., G. Schubert, and D. Brinkman (2001), Small-scale gravity waves in the upper mesosphere and lower thermosphere generated by deep tropical convection, *J. Geophys. Res.*, *106*(D23), 31,825–31,832.

Walterscheid, R. L., J. H. Hecht, R. A. Vincent, I. M. Reid, J. Woithe, and M. P. Hickey (1999), Analysis and interpretation of airglow and radar observations of quasi-monochromatic gravity waves in the upper mesosphere and lower thermosphere over Adelaide, Australia, *J. Atmos. Sol. Terr. Phys.*, *61*(6), 461–478.

Wang, D. Y., and T. F. Tuan (1988), Brunt-Doppler ducting of small period gravity waves, *J. Geophys. Res.*, *93*(A9), 9916–9926.

Waterscheid, R. L., and M. P. Hickey (2011), Group velocity and energy flux in the thermosphere: Limits on the validity of group velocity in a viscous atmosphere, *J. Geophys. Res.*, *116*, D12101, doi:10.1029/2010JD014987.

Yigit, E., A. D. Aylward, and A. S. Medvedev (2008), Parameterization of the effects of vertically propagating gravity waves for thermosphere general circulation models: Sensitivity study, *J. Geophys. Res.*, *113*, D19106, doi:10.1029/2008JD010135.

Yu, Y., and M. P. Hickey (2007a), Numerical modeling of a gravity wave packet ducted by the thermal structure of the atmosphere, *J. Geophys. Res.*, *112*, A06308, doi:10.1029/2006JA012092.

Yu, Y., and M. P. Hickey (2007b), Time-resolved ducting of atmospheric acoustic-gravity waves by analysis of the vertical energy flux, *Geophys. Res. Lett.*, *34*, L02821, doi:10.1029/2006GL028299.

Zhang, S. D., and F. Yi (2002), A numerical study of propagation characteristics of gravity wave packets propagating in a dissipative atmosphere, *J. Geophys. Res.*, *107*(D14), 4222, doi:10.1029/2001JD000864.